

Controlling spin relaxation in hexagonal BN-encapsulated graphene with a transverse electric field

M. H. D. Guimarães,* P. J. Zomer, J. Ingla-Aynés, J. C. Brant, N. Tombros, and B. J. van Wees
Physics of Nanodevices, Zernike Institute for Advanced Materials, University of Groningen, The Netherlands
 (Dated: September 8, 2018)

We experimentally study the electronic spin transport in hBN encapsulated single layer graphene nonlocal spin valves. The use of top and bottom gates allows us to control the carrier density and the electric field independently. The spin relaxation times in our devices range up to 2 ns with spin relaxation lengths exceeding 12 μm even at room temperature. We obtain that the ratio of the spin relaxation time for spins pointing out-of-plane to spins in-plane is $\tau_{\perp}/\tau_{\parallel} \approx 0.75$ for zero applied perpendicular electric field. By tuning the electric field this anisotropy changes to ≈ 0.65 at 0.7 V/nm, in agreement with an electric field tunable in-plane Rashba spin-orbit coupling.

PACS numbers: 72.80.Vp, 72.25.-b, 85.75.Hh

Keywords: Graphene, spin transport, Rashba spin-orbit interaction, anisotropic spin relaxation, Hanle precession, electric field

The generation, manipulation and detection of spin information has been the target of several studies due to the implications for novel spintronic devices [1, 2]. In the recent years graphene has attracted a lot of attention in spintronics due to its theoretically large intrinsic spin relaxation time and length of the order of $\tau_s \approx 100$ ns and $\lambda_s \approx 100$ μm respectively [4, 9]. Although experimental results still fall short of these expectations [3–5, 7], graphene has already achieved the longest measured nonlocal spin relaxation length [5, 9] and furthest transport of spin information at room temperature [10]. However, the mechanisms for spin relaxation in graphene are still under heavy debate with various theoretical models proposed [4, 8, 9, 11–13].

To take advantage of the long spin relaxation times in graphene, e.g. for spin logic devices, one requires easy control of the spin information, for example by an applied electric field. Single layer graphene is an ideal system for this purpose, not only because of its high mobilities and low intrinsic spin-orbit fields (SOF), but also due to the simple relation between the carriers' wavevector, the applied perpendicular electric field and the induced Rashba SOF [4, 7, 9, 15–19]. In bilayer graphene a more complicated behavior is expected when spin-orbit coupling is considered [21].

Here we report nonlocal spin transport measurements on single layer graphene in which we address both topics specified above. Our devices consist of a single layer graphene flake on hexagonal Boron Nitride (hBN) of which a central region is encapsulated with another hBN flake and hence protected from the environment. The presence of a top and bottom gate give rise to two independent electric fields that are experienced by the graphene: $E_{tg} = -\epsilon_{tg}(V_{tg} - V_{tg}^0)/d_{tg}$ and $E_{bg} = \epsilon_{bg}(V_{bg} - V_{bg}^0)/d_{bg}$, respectively [22], where $\epsilon_{tg(bg)} \approx 3.9$ is the dielectric constant, $d_{tg(bg)}$ is the dielectric thickness and $V_{tg(bg)}^0$ the position of the charge neutrality point for the top (bottom) gate. Their difference controls the car-

rier density in the graphene ($n = (E_{bg} - E_{tg})\epsilon_0/e$) and their average gives the effective electric field experienced by the graphene ($\bar{E} = (E_{tg} + E_{bg})/2$), which breaks the inversion symmetry in the encapsulated region, where ϵ_0 is the electric constant and e the electric charge. Our devices show enhanced spin relaxation times of at least 2 ns and also, due to the higher electronic mobility, spin relaxation lengths above 12 μm at room temperature (RT) and 4.2 K. By a simple model we show that the measured spin relaxation times are a lower bound due to the influence of the non-encapsulated regions.

By comparing the spin relaxation time for spins out-of-plane (τ_{\perp}) to spins in-plane (τ_{\parallel}) as a function of the electric field we get insight on the nature of the SOF that cause spin relaxation in graphene. For SOF pointing preferentially in the graphene plane, e.g. for adatoms and impurities, we expect: $\tau_{\perp} \approx 0.5\tau_{\parallel}$ [2, 7, 9, 23]. If the SOF point out-of-plane, as for ripples[9], we have: $\tau_{\perp} \gg \tau_{\parallel}$. However, if the main relaxation mechanism is through random magnetic impurities or defects, no preferential direction for the spins is expected: $\tau_{\parallel} \approx \tau_{\perp}$. Here we obtain $\tau_{\perp}/\tau_{\parallel} \approx 0.75$ at $\bar{E} = 0$ V/nm⁻¹. This ratio decreases with increasing \bar{E} , in agreement with an electric field induced Rashba SOF pointing in the graphene plane.

Device number 1 is illustrated in Fig. 1a and b. The hBN-graphene-hBN stack sits on a 300 nm thick SiO₂ layer on a heavily doped Si substrate which is used as a back-gate. The sample preparation is described in detail in the supplementary information and follows Ref. [1, 2]. We use Co electrodes with a thin TiO₂ interface barrier to perform spin transport measurements. Three devices were studied, all showing similar results. Here we show the results for the device with the longest encapsulated region (≈ 12 μm) and spacing between the inner contacts (13.8 μm).

The charge transport properties of the encapsulated region are measured by applying a current between elec-

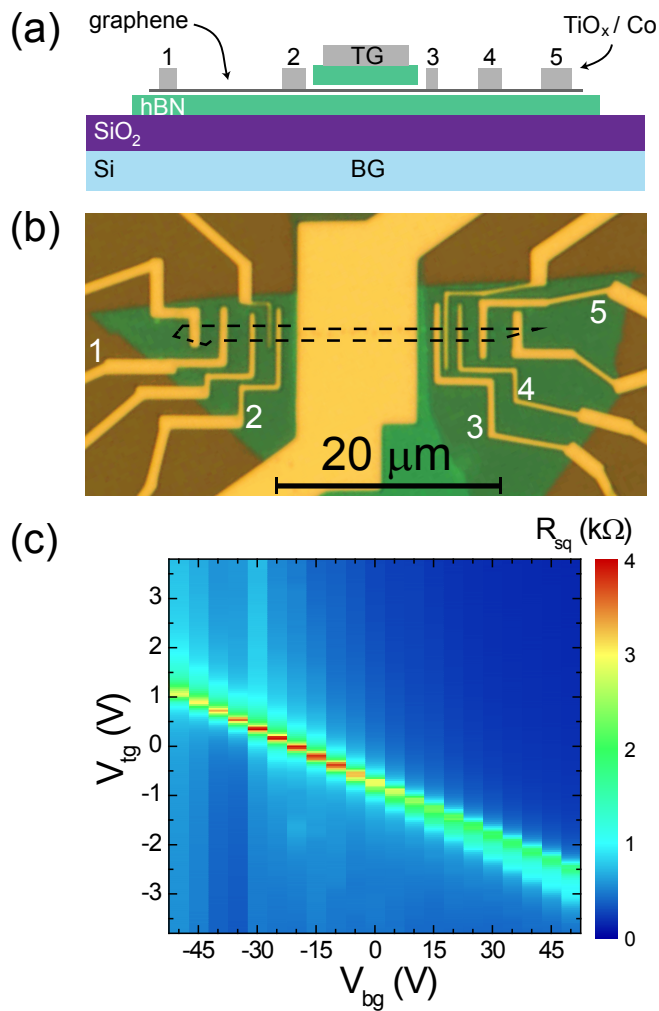


FIG. 1. (a) Side-view schematics and (b) Top-view optical microscope image of a hBN encapsulated graphene spin-valve. The numbers show the contact electrodes and the top (bottom) gates electrodes are indicated as TG (BG). The graphene is outlined by the dashed line. (c) Square resistance (R_{sq}) as a function of V_{tg} and V_{bg} .

trodes 1 and 5, Fig. 1a and b, and scanning the top and bottom gate voltages (V_{tg} and V_{bg} , respectively) while recording the voltage between electrodes 2 and 3. Fig. 1c shows the square resistance (R_{sq}) as a function of V_{tg} and V_{bg} . The charge neutrality point depends on both V_{tg} and V_{bg} in a linear fashion. The slope of the line gives the ratio between the bottom and top gate capacitances: $\alpha_{bg}/\alpha_{tg} \approx 0.036$. A small top gate independent resistance peak around $V_{bg} = -16.6$ V (not visible in Fig. 1c) arises from the non-top gated regions between the two inner contacts. The electronic mobility for this device is $\mu \approx 1.5$ m²/Vs at RT and $\mu \approx 2.3$ m²/Vs at 4.2 K. Although the mobilities of our devices are above the best devices based on SiO₂ they are still one order of magnitude lower than the best devices on hBN [1] which can be attributed to small bubbles or contamination visible

on the graphene/hBN stack.

Spin dependent measurements are performed using a standard nonlocal geometry in which the current path is separated from the voltage detection circuit [4]. The current is driven between electrodes 1 and 2 and the voltage measured between electrodes 3 and 5, which are on the other side of the encapsulated region (Fig. 1a and b). To obtain the spin relaxation time (τ_s) and the spin diffusion coefficient (D_s) we perform Hanle precession measurements where the nonlocal signal is measured as a function of a perpendicular magnetic field B . We then fit the data with the solution to the Bloch equations [4].

The results for D_s , τ_s and the spin relaxation length ($\lambda_s = \sqrt{D_s \tau_s}$) as a function of the V_{tg} for three values of V_{bg} at 4.2 K are shown in Fig. 2. A similar set of measurements was performed at RT and for other samples where only a small difference was observed (see supplementary information [26]).

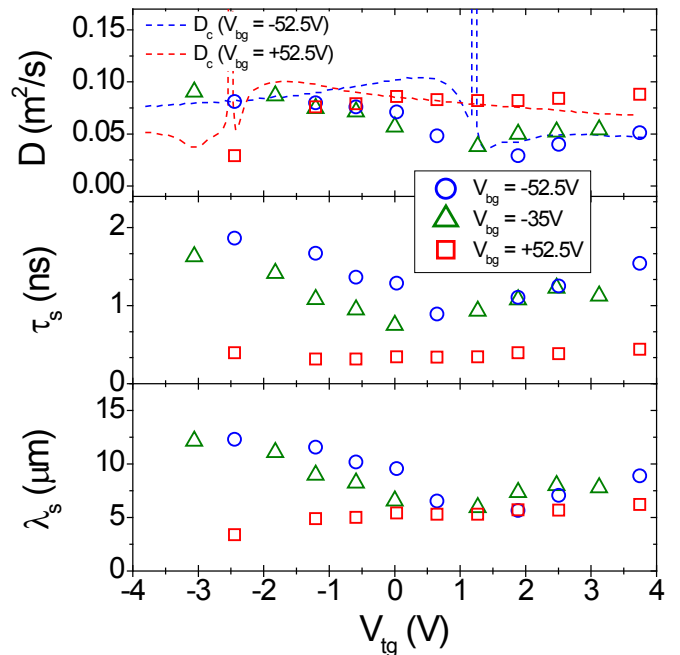


FIG. 2. (Spin) diffusion coefficient (D_s), spin relaxation time τ_s and spin relaxation length λ_s as a function of V_{tg} for three different values of V_{bg} . The error bars are smaller than the dot size. The dashed red (blue) lines show the charge diffusion coefficient D_c for $V_{bg} = +52.5$ V (-52.5 V).

Due to our device mobility, D_s is higher than for regular graphene devices on SiO₂ ($D_s \approx 0.02$ m²/s) [4, 5] and comparable to suspended [3] and non-encapsulated hBN supported devices [10] ($D_s \approx 0.05$ m²/s). As an extra confirmation, we check that D_s agrees with the charge diffusion coefficient $D_c = [R_{sq} e^2 \nu(E_F)]^{-1}$ [27], where e is the electron charge and $\nu(E_F)$ the density of states at the Fermi energy E_F . Next, we observe that the obtained spin relaxation times are higher than those on regular SiO₂ substrates ($\tau_s \approx 0.1 - 1$ ns) [4, 5] and in

non-encapsulated hBN supported devices ($\tau_s \approx 0.1 - 0.5$ ns) [10], reaching up to $\tau_s = (1.9 \pm 0.2)$ ns at 4.2 K and $\tau_s = (2.4 \pm 0.4)$ ns for RT. These values surpass all previous nonlocal measurements of τ_s in single layer graphene both at room and low temperatures [28] [29]. We obtain a maximum of $\lambda_s = 12.3 \mu\text{m}$ at 4.2 K and $\lambda_s = 12.1 \mu\text{m}$ at RT.

Comparing τ_s obtained in our devices with non-encapsulated hBN based devices ($\tau_s \approx 0.2$ ns) [10], we can conclude that the encapsulation of graphene on hBN significantly increases the spin relaxation times. Note that the non-encapsulated devices had comparable electronic mobilities which indicates that τ_s is not linked to the momentum relaxation time in a trivial manner [30]. By measuring a region about $5 \mu\text{m}$ away from the encapsulated part, we find $D_s \approx 0.03 \text{ m}^2/\text{s}$, $\tau_s \approx 0.3$ ns and $\lambda_s \approx 3 \mu\text{m}$, in agreement with the previously reported results. The increase in τ_s for the encapsulated region can be due to several factors. This region is protected from polymer remains or other contamination which can increase spin scattering. In addition to that, the inversion asymmetry, which can generate an extra term for the spin-orbit coupling, is also reduced and controlled by tuning V_{tg} and V_{bg} separately as explained earlier.

As can be seen in Fig. 2, τ_s is modulated by V_{tg} , showing a dip close to the charge neutrality point in the encapsulated region (e.g. $V_{tg} = 1.1$ V and $V_{bg} = -52.5$ V). For larger charge carrier densities in the non-encapsulated regions, the modulation in τ_s by V_{tg} is smaller, although still present. Furthermore, the average value of τ_s is maximum at low carrier densities in the non-encapsulated regions (large negative V_{bg}) and decreases with increasing V_{bg} . This difference on the measured τ_s for different carrier densities on the outer regions can be explained by simulations that treat the full device [3]. Since the transport is diffusive, the spins can explore both the encapsulated and the non-encapsulated regions before being detected. We take this into account by describing our sample as two outer regions connected by a central region [26]. The relevant parameters (R_{sq} , D_s and τ_s) are set for each region individually. The values for the outer regions and R_{sq} and D_s for the inner region can be extracted from our charge and spin transport measurements.

Changing the values of the spin relaxation time for the outer regions, τ_o , around the experimentally obtained values and changing the values for the spin relaxation time in the inner region, τ_i , we simulate Hanle precession curves that are fitted in the same way done for our experiments to obtain an effective value for the spin relaxation time τ_{fit} . We get a reasonable quantitative agreement between our simulations and experiment at $V_{bg} = -52.5$ V for $\tau_i = 3$ ns. This means that the spin relaxation time for the encapsulated region is higher ($\tau_s \approx 3$ ns), but still within the same order of magnitude as the values obtained by analyzing the data using a homogeneous system (Fig. 2). The trend in V_{tg} is also reproduced, which

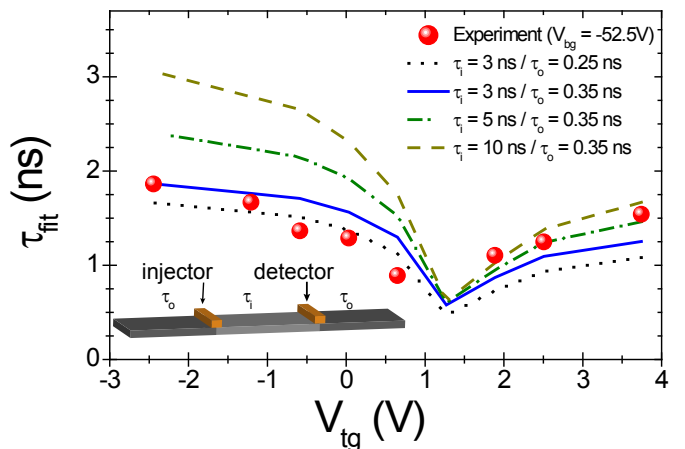


FIG. 3. Effective spin relaxation times extracted for different values for τ_o and τ_i (lines) compared to our experimental data for $V_{bg} = -52.5$ V (dots). The inset shows a schematics of the simulated system.

indicates that it is given by the ratio of the resistivities of the inner and outer regions.

Even though the experimentally obtained value for τ_s depends on the gate voltages in a non-trivial way due to the influence of the non-encapsulated regions, we can still study how the electric field affects the ratio between the spin relaxation times for out-of-plane to in-plane spins: $r = \tau_{\perp} / \tau_{\parallel}$. As explained in the introduction, this way we can get insight about the SOF in our system.

To compare the spin relaxation for spins parallel and perpendicular to the graphene plane we perform the Hanle precession measurements as described before, but increase the perpendicular magnetic field to higher values, $B > 1$ T. At such high magnetic fields the magnetization of the electrodes rotates out-of-plane and the injected spins do not precess anymore. This is seen as a saturation of the nonlocal signal at high B, Fig. 4a.

We observe that different combinations of V_{tg} and V_{bg} result in a saturation of R_{nl} at high magnetic fields at values always smaller than R_{nl} at $B=0$ T, with the saturation occurring at 43-57% of the initial value. Given that the nonlocal spin signal is given by $\Delta R_{nl} = \frac{P^2 R_{sq} \lambda_s}{W} e^{-L/\lambda_s}$, where P is the polarization of the electrodes, L the distance between electrodes and W the channel width, we can estimate the anisotropy in the spin relaxation times assuming that P and R_{sq} do not change significantly with field. Due to a large magnetoresistance at low carrier densities, our analysis is done only for points at large enough carrier densities for both the inner and outer regions [31]. We can relate the ratio of the nonlocal spin signal and the ratio of the spin relaxation times by: $R_{nl}^{\perp} / R_{nl}^{\parallel} = \sqrt{r} e^{\frac{L}{\lambda_{\parallel}} \left(\frac{\sqrt{r}-1}{\sqrt{r}} \right)}$, where $\lambda_{\parallel} = \sqrt{D_s \tau_{\parallel}}$ is obtained via our Hanle precession measurements. In Fig. 4b we plot the ratio $\tau_{\perp} / \tau_{\parallel}$ as a function of \vec{E} for different values of n where we see a clear

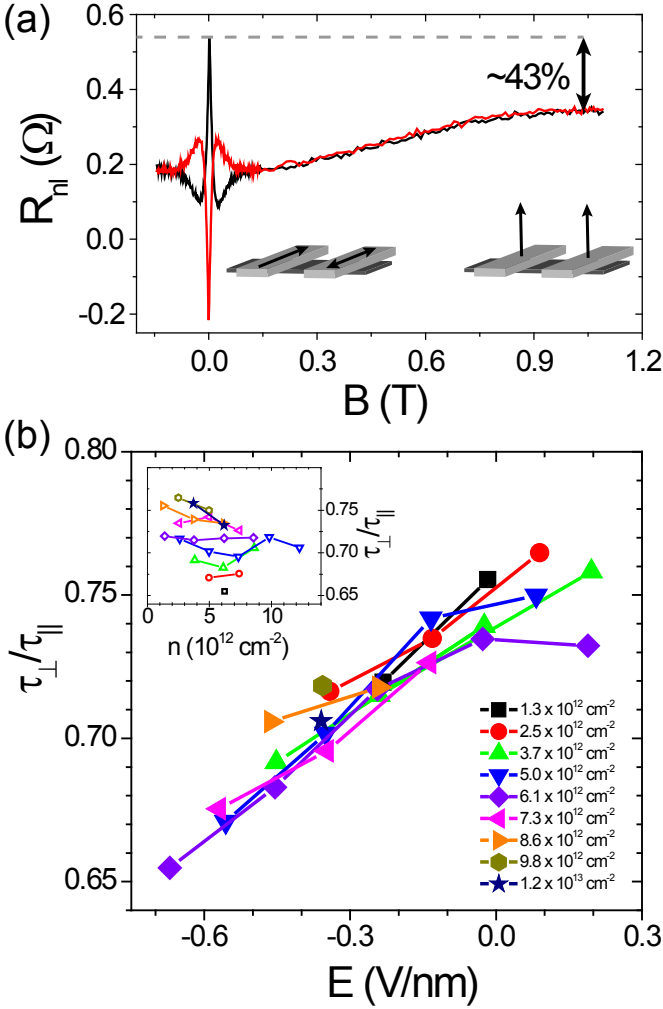


FIG. 4. (a) R_{Hl} as a function of B showing Hanle precession at low fields and a saturation of the signal at high fields when the magnetization of the electrodes point out-of-plane. Inset: A cartoon showing the magnetization of the contacts: in-plane at low fields and out-of-plane at high fields. (b) The ratio $\tau_{\perp}/\tau_{\parallel}$ as a function of electric field \bar{E} for different values of carrier density n . Inset: The same data points for $\tau_{\perp}/\tau_{\parallel}$ used in the main graph, but plotted as a function of n where different colors and symbols represent the different values of \bar{E} .

decrease of this ratio, from 0.75 at $\bar{E} \approx 0$ V/nm to about 0.65 at $\bar{E} \approx -0.7$ V/nm. The inset on Fig. 4b shows the dependence of r as a function of n for different values of \bar{E} where no clear trend can be seen. The value for $\tau_{\perp}/\tau_{\parallel}$ for zero electric field is similar to the values found previously on SiO₂ based devices ($\tau_{\perp} \approx 0.8 \tau_{\parallel}$) [23]. In the case of a inversion symmetric graphene layer with no extrinsic sources for SOF we would not expect any particular preference for direction of the spins, meaning that $\tau_{\perp} \approx \tau_{\parallel}$ [2]. The fact that even at $\bar{E} = 0$ V/nm the ratio between τ_{\perp} and τ_{\parallel} is below 1 means that even without an externally applied electric field there are probably remanent SOF pointing preferentially in the graphene plane.

The decrease of r with increasing \bar{E} is in agreement with theories that dictate an increase in in-plane Rashba SOF with the increase of electric field [4, 7, 15–19]. The Rashba-type spin-orbit Hamiltonian for graphene is given by: $\mathcal{H}_{SO} = \frac{\Delta_R}{2} (\sigma \times \mathbf{s})_z$, where σ and \mathbf{s} are the pseudospin and real spin Pauli matrices respectively. For single layer graphene the spin-orbit constant is known to depend on the \bar{E} in a linear way $\Delta_R = \zeta \bar{E}$ [15, 19], where ζ is the coupling constant. Theoretical values range from $\zeta = 0.3 - 66 \mu\text{eV}/\text{Vnm}^{-1}$ [15–18]. We can roughly estimate ζ by assuming a D'Yakonov-Perel mechanism for spin relaxation [7, 32] with different values for the spin orbit coupling for in- and out-of-plane spins. Our analysis [26] results in $\zeta \approx (40 \pm 20) \mu\text{eV}/\text{Vnm}^{-1}$, within the range of the theoretical predictions.

In conclusion, we measured the spin transport characteristics of a single layer graphene device encapsulated with hBN. We measured spin relaxation times up to $\tau_s \approx 2$ ns and spin relaxation lengths above $\lambda_s = 12 \mu\text{m}$. By taking into consideration that the non-encapsulated regions of our devices play a role in our measurements of τ_s , we estimate the actual spin relaxation time in the encapsulated region to be $\tau_s \approx 3$ ns. Furthermore, we showed that the ratio between out-of-plane and in-plane spin relaxation times changes from $\tau_{\perp}/\tau_{\parallel} \approx 0.75$ to 0.65 with increasing the applied out-of-plane electric field. This observation is in agreement with an electric field induced Rashba-type spin orbit. Our results show not only that τ_s in graphene can be improved by improving the quality of the devices, but also that electrical control of spin information in graphene is possible, paving the way to new graphene spintronic devices.

Note added: During the preparation of this manuscript we became aware of a work in which λ_s up to 10 μm for single and few-layer graphene were achieved for a single gated structure which did not allow the study of τ_s as a function of \bar{E} [33].

We would like to acknowledge A. Kamerbeek and E. Sherman for insightful discussions and J. G. Holstein, H. M. de Roos and H. Adema for the technical support.

The research leading to these results has received funding from the Dutch Foundation for Fundamental Research on Matter (FOM), the European Union Seventh Framework Programme under grant agreement n°604391 Graphene Flagship, the People Programme (Marie Curie Actions) of the European Union's Seventh Framework Programme FP7/2007-2013/ under REA grant agreement n°607904-13 Spinograph, NWO, NanoNed, the Zernike Institute for Advanced Materials and CNPq, Brazil.

* m.h.diniz.guimaraes@rug.nl

[1] S. A. Wolf, D. D. Awschalom, R. A. Buhrman, J. M.

- Daughton, S. von Molnr, M. L. Roukes, A. Y. Chtchelkano, and D. M. Treger, *Science* **294**, 1488 (2001).
- [2] J. Fabian, A. Matos-Abiague, C. Ertler, P. Stano, and I. Zutic, *Acta Physica Slovaca* **57**, 565 (2007).
- [9] D. Huertas-Hernando, F. Guinea, and A. Brataas, *Phys. Rev. Lett.* **103**, 146801 (2009).
- [4] V. K. Dugaev, E. Y. Sherman, and J. Barnaś, *Phys. Rev. B* **83**, 085306 (2011).
- [4] M. Popinciuc, C. Józsa, P. J. Zomer, N. Tombros, A. Veligura, H. T. Jonkman, and B. J. van Wees, *Phys. Rev. B* **80**, 214427 (2009).
- [5] W. Han and R. K. Kawakami, *Phys. Rev. Lett.* **107**, 047207 (2011).
- [7] T.-Y. Yang, J. Balakrishnan, F. Volmer, A. Avsar, M. Jaiswal, J. Samm, S. R. Ali, A. Pachoud, M. Zeng, M. Popinciuc, G. Güntherodt, B. Beschoten, and B. Özyilmaz, *Phys. Rev. Lett.* **107**, 047206 (2011).
- [3] M. H. D. Guimarães, A. Veligura, P. J. Zomer, T. Maassen, I. J. Vera-Marun, N. Tombros, and B. J. van Wees, *Nano Letters* **12**, 3512 (2012).
- [9] M. Wojtaszek, I. J. Vera-Marun, T. Maassen, and B. J. van Wees, *Phys. Rev. B* **87**, 081402 (2013).
- [10] P. J. Zomer, M. H. D. Guimarães, N. Tombros, and B. J. van Wees, *Phys. Rev. B* **86**, 161416 (2012).
- [11] D. Kochan, M. Gmitra, and J. Fabian, *Phys. Rev. Lett.* **112**, 116602 (2014).
- [12] P. Zhang and M. W. Wu, *New Journal of Physics* **14**, 033015 (2012).
- [13] S. Roche and S. O. Valenzuela, *Journal of Physics D: Applied Physics* **47**, 094011 (2014).
- [8] H. Ochoa, A. H. Castro Neto, and F. Guinea, *Phys. Rev. Lett.* **108**, 206808 (2012).
- [15] M. Gmitra, S. Konschuh, C. Ertler, C. Ambrosch-Draxl, and J. Fabian, *Phys. Rev. B* **80**, 235431 (2009).
- [16] D. Huertas-Hernando, F. Guinea, and A. Brataas, *Phys. Rev. B* **74**, 155426 (2006).
- [17] C. L. Kane and E. J. Mele, *Phys. Rev. Lett.* **95**, 226801 (2005).
- [18] H. Min, J. E. Hill, N. A. Sinitsyn, B. R. Sahu, L. Kleinman, and A. H. MacDonald, *Phys. Rev. B* **74**, 165310 (2006).
- [19] E. I. Rashba, *Phys. Rev. B* **79**, 161409 (2009).
- [7] C. Ertler, S. Konschuh, M. Gmitra, and J. Fabian, *Phys. Rev. B* **80**, 041405 (2009).
- [21] S. Konschuh, M. Gmitra, D. Kochan, and J. Fabian, *Phys. Rev. B* **85**, 115423 (2012).
- [22] Y. Zhang, T.-T. Tang, C. Girit, Z. Hao, M. C. Martin, A. Zettl, M. F. Crommie, Y. R. Shen, and F. Wang, *Nature* **459**, 820 (2009).
- [23] N. Tombros, S. Tanabe, A. Veligura, C. Jozsa, M. Popinciuc, H. T. Jonkman, and B. J. van Wees, *Phys. Rev. Lett.* **101**, 046601 (2008).
- [1] L. Wang, I. Meric, P. Y. Huang, Q. Gao, Y. Gao, H. Tran, T. Taniguchi, K. Watanabe, L. M. Campos, D. A. Muller, J. Guo, P. Kim, J. Hone, K. L. Shepard, and C. R. Dean, *Science* **342**, 614 (2013).
- [2] P. J. Zomer, M. H. D. Guimares, J. C. Brant, N. Tombros, and B. J. van Wees, *Applied Physics Letters* **105**, 013101 (2014).
- [26] “See supplemental material at prl.aps.org for a detailed description of the device fabrication, transport measurements, simulation of spin transport in inhomogeneous systems, analysis of the experimental data, results for different samples and temperatures and the estimation of the electric field dependent spin-orbit coupling.”.
- [27] A resistance of 3.2 k Ω was subtracted in the calculation of D_c for $V_{bg} = -52.5\text{V}$ to account for the non-top gated regions.
- [28] 2-terminal local measurements on epitaxial graphene estimated $\tau_s \approx 100$ ns at 4.2 K [29].
- [29] B. Dlubak, M.-B. Martin, C. Deranlot, B. Servet, S. Xavier, R. Mattana, M. Sprinkle, C. Berger, W. A. De Heer, F. Petroff, A. Anane, P. Seneor, and A. Fert, *Nat Phys* **8**, 557 (2012).
- [30] W. Han, J.-R. Chen, D. Wang, K. M. McCreary, H. Wen, A. G. Swartz, J. Shi, and R. K. Kawakami, *Nano Letters* **12**, 3443 (2012), <http://pubs.acs.org/doi/pdf/10.1021/nl301567n>.
- [31] At low n , R_{sq} of our devices scales with B^2 leading to a background in our signal that overcomes the nonlocal spin signal at large B .
- [32] M. D’Yakonov and V. Perel’, *Soviet Journal of Experimental and Theoretical Physics* **33**, 1053 (1971).
- [33] M. Droegeler, F. Volmer, M. Wolter, B. Terres, K. Watanabe, T. Taniguchi, G. Guntherodt, C. Stampfer, and B. Beschoten, “Nanosecond spin lifetimes in single- and few-layer graphene-hbn heterostructures at room temperature,” (2014), arXiv:arXiv:1406.2439.

SUPPLEMENTAL MATERIAL: CONTROLLING SPIN RELAXATION IN HEXAGONAL BN-ENCAPSULATED GRAPHENE WITH A TRANSVERSE ELECTRIC FIELD

Fabrication of the stacks

The hBN-graphene-hBN stacks were fabricated using a pick-up method [1] described elsewhere [2] in more details. The graphene and hBN flakes were obtained by mechanical cleavage of HOPG (SPI Supplies) and hBN powder (HQ Graphene). The preparation of the stacks starts with the exfoliation and optical microscopy selection of hBN on a glass mask covered by a thin layer of polycarbonate (HQ Graphene). The single layer graphene and bottom hBN flakes are exfoliated on Si/SiO₂ substrates and selected by optical microscopy. The mask containing the top hBN flake is then aligned and pressed against the substrate containing the graphene flake and heated to ≈ 75 °C. When the mask is retracted from the substrate the graphene flake adheres strongly to the hBN flake and releases from the substrate sticking to the mask. The mask containing the hBN-graphene stack is then aligned to the bottom hBN flake, brought in contact to the substrate and heated to temperatures up to ≈ 150 °C. At these temperatures the polycarbonate film melts on the substrate and releases from the mask together with the stack. The sample is then left in chloroform for at least 15 hours in order to completely dissolve the polycarbonate film and obtain a clean graphene surface ensuring good graphene-contact interfaces.

Contact deposition

The contacts and top gate electrodes in this work were all fabricated at the same step to avoid further contamination of the non-encapsulated graphene regions. The electrodes were patterned using standard e-beam lithography techniques using a PMMA 950K (270 nm thick) resist. The markers for the e-beam lithography were patterned prior to the electrodes in the same PMMA resist and developed leaving openings which were used for the alignment of the electrodes. We then used an e-beam evaporator with a base pressure below 10^{-6} Torr to evaporate a 0.4 nm thick layer of Ti which was then naturally oxidized by inserting pure oxygen gas in the vacuum chamber to achieve pressures above 1 Torr. After 15 minutes the chamber was pumped down once again to the initial base pressure and the procedure was repeated to deposit and oxidize another 0.4 nm thick Ti layer. This procedure is then followed by the deposition of a 67 nm thick Co layer with a capping layer of Al (5 nm) to protect the Co layer from oxidizing. The large thickness of the Co layer is necessary to both overcome the height of the bottom hBN flake and also to facili-

tate the alignment of the electrodes by the perpendicular magnetic field. After the resist lift-off and wire bonding, the samples were loaded in a continuous He flow cryostat which stands in a room temperature electro-magnet. The contact resistances were in the range 2 - 100 k Ω .

Transport measurements

The charge transport measurements were performed by standard low-frequency lock-in techniques with currents up to 100 nA. All spin transport measurements presented here were done using the non-local geometry in which the charge contribution to the measured signal is minimized by separating the charge current path from the voltage detection circuit. We used standard low-frequency lock-in techniques with applied currents of 1 μ A in order to preserve the high resistive contact interface barriers and avoid device heating.

Magnetoresistance effects on the nonlocal signal

To be sure that the magneto-resistance contribution is minimal in our nonlocal signals we characterize the graphene sheet resistance as a function of the applied magnetic field. In Fig. 5 we show a typical curve of the R_{sq} versus V_{tg} for $B = 0$ and 1 T measured in a 4-probe geometry. It can be seen that the change in R_{sq} with B is maximum around the charge neutrality point and small at high values of n . This observation also reflects on our nonlocal measurements in which we observe the monotonic increase in the nonlocal resistance as a function of B characteristic to magneto-resistance effects only for low n .

Simulation of Hanle precession data for non-homogeneous systems

In order to describe the different regions in our system (encapsulated and non-encapsulated) we use a model for spin transport in an inhomogeneous system described elsewhere [3]. We solve the Bloch equations for spin diffusion in one dimension for a system with three distinct regions connected to one another. Each one of these regions can have independent values for the relevant parameters. We assume the outer regions identical, with square resistance R_o , spin diffusion coefficient D_o and spin relaxation time τ_o . The inner region has distinct parameters R_i , D_i and τ_i . We assume that the spins are injected at the left boundary of the inner region and detected on the right, which results in a nonlocal spin signal R_{sim} . For this work we get R_o , D_o , τ_o , R_i and D_i by charge and spin transport experiments as described in the main text. We then fit the simulated curves for

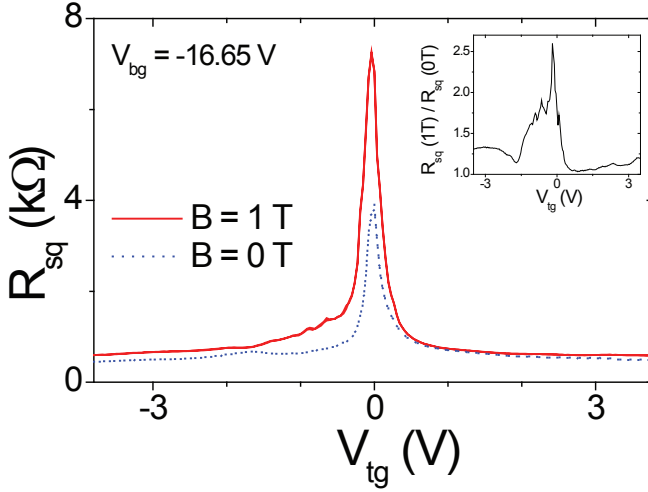


FIG. 5. Graphene square resistance as a function of V_{tg} for $V_{bg} = -16.65$ V for sample 1 at 4.2 K and $B = 0$ (dashed blue line) and 1 T (red solid line). *Inset*: Ratio between the two curves in the main graph showing the magneto-resistance in the sample.

R_{sim} using the solution for the Bloch equation for homogeneous systems (exactly in the same way we analyze our experimental results). From this fit we extract an effective spin diffusion coefficient D_{fit} and relaxation time τ_{fit} . An example of such simulated curve and fitting is shown in Fig. 6.

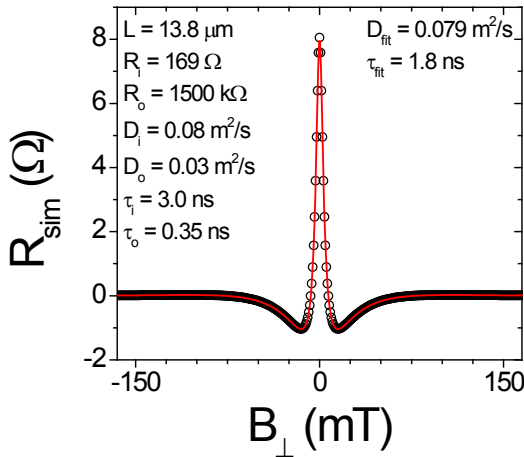


FIG. 6. Hanle precession curve calculated using the model for a non-homogeneous system (black dots) with a fit using the expression for the solution of the Bloch equation in a homogeneous system.

For a fixed V_{bg} , the effect of V_{tg} is to change the spin resistance ratio between the inner and outer regions, $\frac{R_i \lambda_i}{R_o \lambda_o}$, where $\lambda_{i(o)}$ is the spin relaxation length for the inner (outer) regions. The change of this ratio affects strongly the extracted spin relaxation times τ_{fit} but leaves D_{fit} mostly unaffected [3]. In order to get a good estimation

of τ_i , we take the experimental values for $V_{bg} = -52.5$ V and simulate a few sets of points with only changing R_i . As it can be seen in Fig. 3b in the main text, we find a close match between our simulated values of τ_{fit} to our experimentally obtained values of τ_s for τ_i ranging from 3 to 5 ns. Meaning that the spin relaxation time for the encapsulated region is higher than, but still within the same order of magnitude of, the experimentally obtained values using the solution for the Bloch equations in a homogeneous system.

It is known that R_c can affect the measurement of τ_s , especially in the case of very long values of λ_s . However, even though we have a wide range of contact resistances R_c 2 - 100 k Ω with one sample having all contact resistances above 50 k Ω , we did not see any clear correlation between R_c and the measured τ_s . We would expect that, in the case of contact induced spin relaxation or poor graphene quality in the regions underneath the contacts, τ_s would be mostly affected in the non-encapsulated regions. Therefore, the measured spin relaxation time for the non-encapsulated will be an effective spin relaxation time that includes all these effects, and consequently is taken into account in our model by setting τ_o as the measured spin relaxation time for these regions.

Experimental Hanle precession data

For most of our devices we observe a small asymmetry in our Hanle precession curves between negative and positive perpendicular magnetic fields 7 which might arise due to some anisotropy in the magnetization of the electrodes. Although we cannot be certain about the reason for this asymmetry, the parameters extracted by fitting just one or the other side of the curve do not change significantly. Comparing the parameters extracted from each side, τ_s deviates by a factor of ≈ 1.06 and D_s by a maximum of a factor 2. Since the values for D_s extracted by fitting the whole Hanle curve match the values for D_c extracted by charge transport measurements, we believe that our procedure is justified.

The measured spin polarization of our electrodes were in the range $P = 1 - 6$ %. These values for P are in the lower range of the values reported in literature [4, 5], however we believe that this value can be improved by increasing the quality of the high resistive barriers [6].

Results for spin and charge transport at 4.2 K and room temperature

Our results presented in the main text were all performed in sample 1 at 4.2 K. For comparison we also include here the square resistance as a function of V_{tg} and V_{bg} and the extracted spin transport parameters for the same sample at room temperature (Fig. ??a) and an-

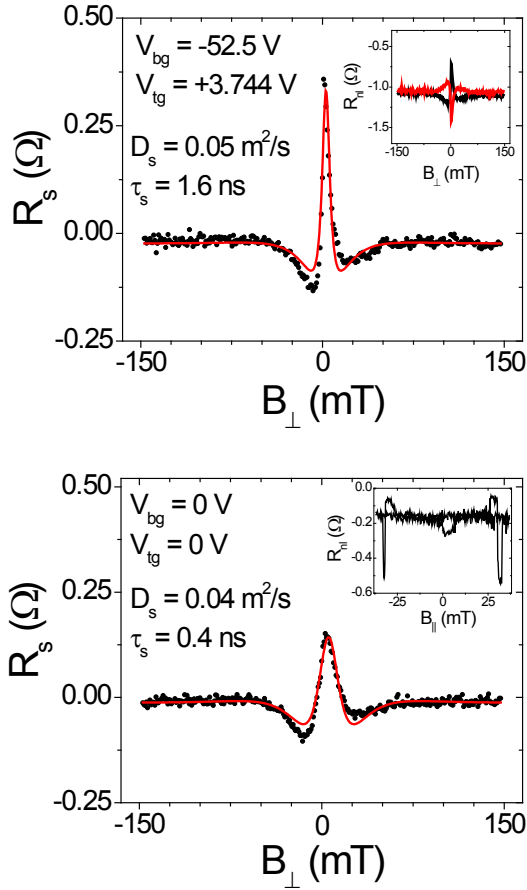


FIG. 7. Top: Experimental data for $R_s = (R_{nl}^P - R_{nl}^{AP})/2$ at $V_{bg} = -52.5$ V and $V_{tg} = +3.744$ V, where $R_{nl}^{P(AP)}$ is the non-local resistance obtained for the electrodes in a (anti)parallel magnetization (dots) as a function of an applied perpendicular magnetic field. The fit (red line) used to extract D_s and τ_s is also shown. In the inset it is shown the data for $R_{nl}^{P(AP)}$ in black (red). Bottom: Hanle precession curve for $V_{bg} = V_{tg} = 0$ V with the respective non-local spin-valve shown in the inset.

other sample (sample 2) at room (Fig. ??b) and liquid Helium (Fig. ??c) temperatures. The samples dimensions and their electronic mobilities at room temperature and 4.2 K are given in table ?. Sample 3 (not shown here) showed similar results.

Estimation of Δ_R

In order to give a rough estimation for the spin orbit coupling strength Δ_R we assume that the spin relaxation is composed of the sum of an electric field independent and electric field dependent terms: $1/\tau_{\perp} = 1/\tau_{ind} + 1/\tau_E$. The spin relaxation time τ_{\parallel} is taken equal to the spin relaxation experimentally (τ_s) and τ_{ind} is τ_s multiplied by the ratio $r = \tau_{\perp}/\tau_s$ at $\bar{E} = 0$ V/nm: $\tau_{ind} = 0.75\tau_s$. If we assume a D'Yakonov-

Perel spin relaxation mechanism for $1/\tau_E = \frac{4\Delta_R^2}{\hbar^2}\tau_p$, we have: $\Delta_R = \zeta\bar{E} = (\hbar/2)(\tau_E\tau_p)^{-1/2}$ [7], where $\tau_p = 2D_c/v_F$ is the momentum relaxation time, D_c the charge diffusion constant and $v_F \approx 10^6$ m/s the Fermi velocity. We further take $D_c \approx D_s$. Solving it for τ_E we have:

$$\tau_E = \tau_s \left(\frac{1}{r} - \frac{1}{0.75} \right)^{-1}, \quad (1)$$

and

$$\zeta = \frac{\Delta_R}{\bar{E}} = \frac{\hbar}{2\bar{E}} \frac{1}{\sqrt{\tau_s\tau_p}} \left(\frac{1}{r} - \frac{1}{0.75} \right)^{-1/2} \quad (2)$$

D'YAKONOV-PEREL *VERSUS* ELLIOTT-YAFET MECHANISMS FOR SPIN RELAXATION

Two mechanisms are often considered in order to try to explain spin relaxation in graphene: they are the D'Yakonov-Perel (DP) and Elliott-Yafet (EY) mechanisms for spin relaxation. These two mechanisms show different behavior of the spin relaxation time as a function of the momentum relaxation time (τ_p): $\tau_{EY} \propto \tau_p$ and $\tau_{DP} \propto 1/\tau_p$, with $\tau_{EY(DP)}$ been the spin relaxation time due to the EY (DP) mechanism.

It was theoretically demonstrated that τ_{EY} for the specific case of graphene for many different type of scatterers is given by [8]:

$$\tau_{EY} \approx \frac{E_F^2}{\Delta_{SO}^2} \tau_p, \quad (3)$$

where E_F is the Fermi energy and Δ_{SO} the spin orbit coupling. The DP mechanism obeys:

$$\tau_{DP} \approx \frac{\hbar^2}{\Delta_{SO}^2} \frac{1}{\tau_p}. \quad (4)$$

Following the reasoning of Huertas-Hernando et al. [9], to obtain the relative importance of these mechanisms we take the ratio:

$$\frac{\tau_{EY}}{\tau_{DP}} \approx \left(\frac{E_F\tau_p}{\hbar} \right)^2. \quad (5)$$

If $\tau_{EY}/\tau_{DP} > 1$, the spin relaxation time due to the DP mechanism is smaller and it dominates over the EY mechanism. Using typical values for our samples of $E_F \approx 30$ meV (equivalent to a charge carrier density $n \approx 10^{12}$ cm $^{-2}$) and $\tau_p \approx 10^{-13}$ s, we obtain $\tau_{EY}/\tau_{DP} \approx 20$, indicating a higher importance of the DP mechanism for the spin relaxation in our samples.

Although this is not a definite proof that the DP is the dominant mechanism for spin relaxation in graphene, we believe that it is the most appropriate way to obtain the spin orbit coupling strength due to the electric field in our devices.

-
- * m.h.diniz.guimaraes@rug.nl
- [1] L. Wang, I. Meric, P. Y. Huang, Q. Gao, Y. Gao, H. Tran, T. Taniguchi, K. Watanabe, L. M. Campos, D. A. Muller, J. Guo, P. Kim, J. Hone, K. L. Shepard, and C. R. Dean, *Science* **342**, 614 (2013).
 - [2] P. J. Zomer, M. H. D. Guimaraes, J. C. Brant, N. Tombros, and B. J. van Wees, *Applied Physics Letters* **105**, 013101 (2014).
 - [3] M. H. D. Guimarães, A. Veligura, P. J. Zomer, T. Maassen, I. J. Vera-Marun, N. Tombros, and B. J. van Wees, *Nano Letters* **12**, 3512 (2012).
 - [4] M. Popinciuc, C. Józsa, P. J. Zomer, N. Tombros, A. Veligura, H. T. Jonkman, and B. J. van Wees, *Phys. Rev. B* **80**, 214427 (2009).
 - [5] W. Han and R. K. Kawakami, *Phys. Rev. Lett.* **107**, 047207 (2011).
 - [6] W. Han, K. Pi, K. M. McCreary, Y. Li, J. J. I. Wong, A. G. Swartz, and R. K. Kawakami, *Phys. Rev. Lett.* **105**, 167202 (2010).
 - [7] C. Ertler, S. Kunschuh, M. Gmitra, and J. Fabian, *Phys. Rev. B* **80**, 041405 (2009).
 - [8] H. Ochoa, A. H. Castro Neto, and F. Guinea, *Phys. Rev. Lett.* **108**, 206808 (2012).
 - [9] D. Huertas-Hernando, F. Guinea, and A. Brataas, *Phys. Rev. Lett.* **103**, 146801 (2009).

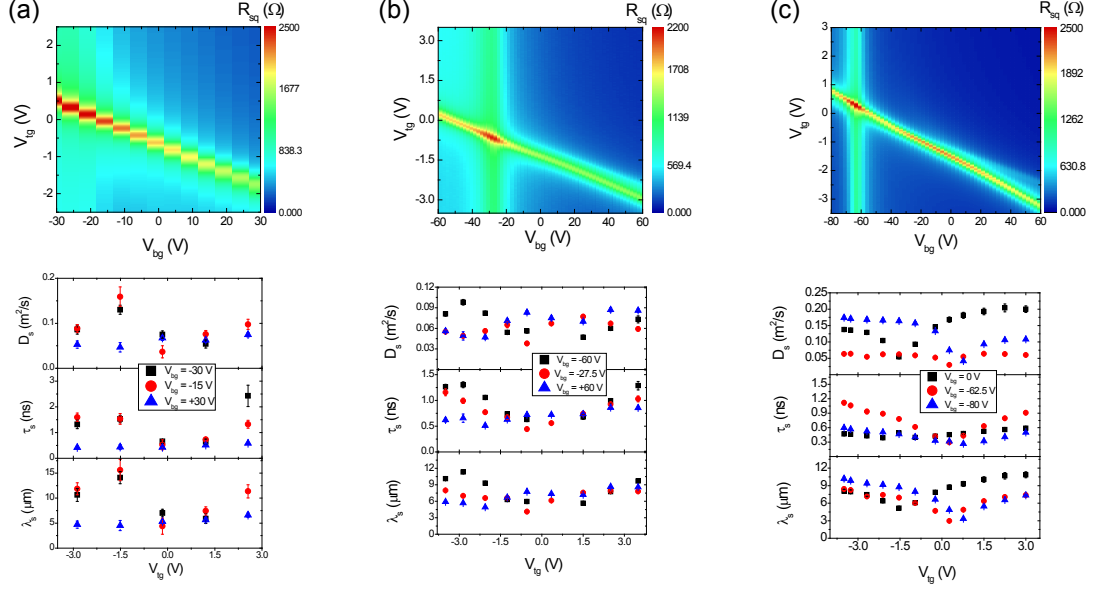


FIG. 8. Charge and spin transport measurements for (a) sample 1 at room temperature and sample 2 at (b) room temperature and (c) 4.2 K.

	ℓ_{tg}	ℓ_{enc}	L	W	μ_{RT}	μ_{4K}
Sample 1	10.35 μm	12 μm	13.8 μm	1.3 μm	1.5 m^2/Vs	2.3 m^2/Vs
Sample 2	4.5 μm	7.6 μm	8.72 μm	2.8 μm	2.4 m^2/Vs	3.3 m^2/Vs

TABLE I. Length of the top gated region (ℓ_{tg}), encapsulated region (ℓ_{enc}), inner electrodes spacing (L), graphene flake width (W) and electronic mobilities at room temperature (μ_{RT}) and 4.2 K (μ_{4K}) for samples 1 and 2.